SAND2023-01857J

2D-imaging of absolute OH and H_2O_2 profiles in a He-H_2O nanosecond pulsed dielectric barrier discharge by photo-fragmentation laser-induced fluorescence

Dirk van den Bekerom[1], Malik M Tahiyat[2], Erxiong Huang[1], Jonathan H Frank[1], and Tanvir I Farouk[2]

[1] Combustion Research Facility, Sandia National Laboratories, Livermore, CA 94551, USA
[2] Department of Mechanical Engineering, University of South Carolina, Columbia, SC 29208, USA

E-mail: tfarouk@sc.edu, jhfrank@sandia.gov

Abstract

Pulsed dielectric barrier discharges (DBD) in He-H_2O and He-H_2O-O_2 mixtures are studied in near atmospheric conditions using temporally and spatially resolved quantitative 2-D imaging of the hydroxyl radical (OH) and hydrogen peroxide (H_2O_2). The primary goal was to detect and quantify the production of these strongly oxidative species in water-laden helium discharges in a DBD jet configuration, which is of interest for biomedical applications such as disinfection of surfaces and treatment of biological samples. Hydroxyl profiles are obtained by laser-induced fluorescence (LIF) measurements using 282 nm laser excitation. Hydrogen peroxide profiles are measured by photo-fragmentation LIF (PF-LIF), which involves photo-dissociating H_2O_2 into OH with a 212.8 nm laser sheet and detecting the OH fragments by LIF. The H_2O_2 profiles are calibrated by measuring PF-LIF profiles in a reference mixture of He seeded with a known amount of H_2O_2. OH profiles are calibrated by measuring OH-radical decay times and comparing these with predictions from a chemical kinetics model. Two different burst discharge modes with 5 and 10 pulses per burst are studied, both with a burst repetition rate of 50 Hz. In both cases, dynamics of OH and H_2O_2 distributions in the afterglow of the discharge are investigated. Gas temperatures determined from the OH-LIF spectra indicate that gas heating due to the plasma is insignificant. The addition of 5% O_2 in the He admixture decreases the OH densities and increases the H_2O_2 densities. The increased coupled energy in the 10-pulse discharge increases OH and H_2O_2 mole fractions, except for the H_2O_2 in the He-H_2O-O_2 mixture which is relatively insensitive to the additional pulses.

Keywords: photo fragmentation laser-induced fluorescence (PF-LIF), hydroxyl, hydrogen peroxide, dielectric barrier discharge, fluorescence spectroscopy

1. Introduction

Nonthermal plasma (NTP) discharges in the presence of water are important in a wide range of research areas, including environmental (*1-3*), biomedical (*4-7*), and catalysis (*8-10*) applications. The primary reason for this broad impact is the production of reactive oxidizing species from NTP discharges in a humid medium, particularly OH, H_2O_2, and O_3, which play active roles in physicochemical processes. In waste water treatment, OH and ozone are the primary species responsible for the oxidation of organic contaminants in liquid (*1*) and gaseous states (*3*). Both OH and H_2O_2 are prominent oxidizers in plasma-activated water that has antibacterial effects (*2, 4*). OH, H_2O_2, and O_3 generated from NTP promote proliferation when the NTP is applied to mammalian cells (*5*). The OH radicals generated from NTP have shown promise in treatment of cancer cells, and H_2O_2 consumption rates of cancer cells have been correlated with the cytotoxicity of plasma treatments (*6, 11*). Plasma-catalytic destruction of volatile organic compounds (VOCs) increases in efficiency due to the formation of OH in the presence of humid air (*8, 10*). Hydroxylation reactions are one of the primary pathways for catalytic breakdown of pharmaceutical wastes (*9*). To understand discharge chemistry and conditions responsible for the generation of these oxidizing species, it is imperative to know their respective distributions within the discharge for different operating parameters.

OH densities are routinely measured by laser-induced fluorescence (LIF), in both flames (*12*) and plasmas for 0-D, (*13-16*), 1-D (*17*), and 2-D measurements (*18-21*). In most cases, a frequency-doubled dye laser is used to generate a 282 nm beam output used for the excitation of OH in the A-X(1,0) band. The laser is synchronized with the high voltage pulser, which enables phase-averaged time resolved measurements by varying the delay between the plasma discharge and laser pulse. Fluorescence around 310 nm from the A-X(1,1) and A-X(0,0) bands is captured by a photomultiplier tube (PMT) or intensified charged coupled device (ICCD) camera, coupled with either a monochromator or narrow bandpass filter. The absolute calibration of the OH mole fraction is performed either via a chemical kinetic model or UV absorption spectroscopy.

Broadband UV absorption spectroscopy utilizing UV LEDs has been used to measure the absolute number densities of OH in radiofrequency (RF) glow discharges having He-H_2O as a feed gas mixture (*22*). The discharge morphology of dielectric barrier discharges (DBD) with H_2O in He and Ar was also investigated via optical emission spectroscopy (OES) imaging and broadband absorption measurements (*23*). The study indicated that differences in the relative concentrations of OH and H_2O for the two bath gases resulted from a change in the number of micro discharge filaments, surface charge density, and kinetic losses. LIF measurements in a pulsed arc discharge in $H_2O/O_2/N_2$ mixtures showed that the OH concentration increased with both humidity and oxygen content due to the formation of additional reaction

pathways (*24*). Spatial and temporal temperature measurements in the afterglow of a pulsed positive corona discharge for a similar gas mixture indicated that the temperature at the anode tip was higher than in the rest of the discharge volume (*25*). This temperature difference resulted in a significantly slower OH decay rate at the anode. In a nozzle-to-plane DC streamer corona discharge, 2-D LIF showed that OH radicals were produced mostly within the streamers and the shape of these streamers was affected by the presence of metastables from associated carrier gases (*26*).

The OH number density was measured in the afterglow of a nanosecond pulsed discharge (NSP) in He and trace amounts of H_2O, with three different techniques for comparison: UV absorption, LIF calibrated with Rayleigh scattering, and LIF calibrated with chemical kinetics modeling (*27*). The results from these techniques agreed with each other to within the experimental uncertainty. The spatial distribution of OH density in a NSP discharge with He-H_2O mixtures was studied with LIF for two different discharge power densities (*18*). The study identified that the contribution of dissociative recombination and charge exchange to the formation of OH radicals can be equally important to that of thermal dissociation and electron-induced dissociation of water.

Most experimental studies of OH in water-laden plasmas involve trace amounts of water vapor in carrier gases: nitrogen (*28*), helium (*18, 23, 29*), argon (*23*), and synthetic air (*24, 25*), but studies involving high water vapor content are very limited. LIF measurements in atmospheric pressure DBD in He-H_2O mixtures have shown that OH densities have a stronger dependence on the water vapor content than on discharge current; the maximum OH number density at saturated vapor pressure was 10^{13} cm^{-3} (*13*). Considering the sensitivity of OH-production to the water content, studies of discharges with moderate and high water content would be of great interest. Even though LIF measurements of OH and the gas temperature in He, N_2, and O_2 gases with trace amounts of water vapor have been well investigated in pulsed DC systems, similar measurements of OH and H_2O_2 in high water content DBD systems have been relatively scarce.

Compared to OH, studies in quantifying H_2O_2 profiles in a plasma have been much less prevalent. Investigations of H_2O_2 produced in plasma-liquid interactions have mostly been limited to the liquid phase, where H_2O_2 concentrations are measured ex-situ by sampling the effluent and using colorimetric methods (*30*). IR-absorption spectroscopy has been used to measure gas-phase H_2O_2 concentrations in other applications, such as shock tube studies (*31*) but yielded only line of sight measurements. In one of the few local in-situ plasma measurements, Pai et al. employed Raman scattering to measure a number of species at the liquid-plasma interface, including H_2O_2 (*32*). The techniques employed to date are mostly limited to ex-situ or line-integrated measurements that do not capture the spatial and temporal evolution of species

and may underestimate or completely miss the highly reactive species that do not survive in the effluent of a plasma reactor.

Imaging measurements of gas-phase H_2O_2 in the context of plasma-liquid interactions are challenging because direct detection by laser-induced fluorescence is precluded by the dissociative nature of the electronically excited states of H_2O_2. One way to measure time-resolved 2D profiles of molecules that do not have available LIF transitions is to first photo-dissociate the molecule of interest into fragments that can then be detected by LIF, a technique called photo-fragmentation LIF (PF-LIF). This pump-probe technique has been applied to several small polyatomic molecules such as H_2O_2 (*33, 34*), CH_3 (*35*), O_3 (*36*), and NO_2 (*37*), mostly in combustion environments but also in plasmas(*38*). To the best of our knowledge, this work is the first application of PF-LIF for the detection of H_2O_2 in a plasma. Hydrogen peroxide has a broad, featureless UV absorption spectrum and can be photo-dissociated over a large range of wavelengths, with the absorption cross-section increasing considerably for shorter wavelengths. At wavelengths below 555 nm, the dominant photo-products are two ground-state OH molecules, which can be easily detected by LIF using a tunable probe laser. However, at shorter wavelengths, additional dissociation channels can become significant, which reduces the yield of ground-state OH (*39*).

A limited number of studies have used photo-fragmentation LIF for qualitative imaging of H_2O_2 in combustion environments. Photo-dissociation of H_2O_2 into two OH molecules can be accomplished using UV wavelengths available from pulsed solid-state and excimer lasers. For example, the fourth harmonic of an Nd:YAG laser (λ = 266 nm) is used to produce OH photo-fragments which are, in turn, excited by LIF and the resulting signals are detected (*33, 34*). Larsson et al. showed that by using a KrF excimer laser at 248 nm for the photo-fragmentation, the H_2O_2 diagnostic can be combined with H_2O detection by performing two-photon absorption LIF (TALIF) on the water molecules (*40*).

In this investigation, we studied the time-evolved generation of OH and H_2O_2 in a near-atmospheric pressure (600 Torr) dielectric barrier discharge in two different carrier gas mixtures: He-H_2O and He-H_2O-O_2, both with saturated water vapor. The planar distributions of H_2O_2 and OH were measured using PF-LIF and LIF, respectively. Helium was used as the carrier gas to minimize reactions that involve OH kinetics, which is expected to facilitate modeling of the discharge and reduces collisional quenching of the electronically excited OH (*29*). The H_2O_2 profile was calibrated by recording PF-LIF images in a He-H_2O-H_2O_2 reference mixture, where the absolute H_2O_2 concentration was determined by UV-absorption of the 212.8 nm photo-fragmentation laser. The OH concentration was calibrated by comparing the decay times of photolytically produced OH in the reference mixture with those predicted by a chemical kinetic model.

The results from these experiments will serve as a validation target for plasma kinetic simulations since such data for high water vapor concentration is not readily available in the literature.

2. Experimental Setup

The schematic of the plasma setup and configuration is shown in **Fig. 1a**. A mixture of He and H_2O is produced by continuously flowing up to 5 slm of He gas through a mass flow controller and into a bubbler containing deionized water in a temperature-controlled water bath maintained at 283 K. The temperature of the water bath is kept 10 K below the room temperature to prevent condensation in the gas lines and mist formation. The resultant He-H_2O mixture flows from the top of the electrode through the center and forms a stagnation flow in the 4 mm interelectrode spacing between the quartz dielectric and a grounded stainless-steel plate. The entire electrode assembly is placed in a 6-way cross quartz cell (see Fig. 2), with the pressure maintained at 600 Torr. A high voltage pulser (TPS SSPG-20X-100K), operating in burst mode, delivers high voltage pulses to the powered electrode. The pulse burst and repetition rate are controlled by a digital delay generator. The 100 μs burst consists of either 5 pulses (50 kHz) or 10 pulses (100 kHz) and is repeated at 20 ms intervals (50 Hz). The delay generator also synchronizes the 10 Hz lasers and the camera with every 5^{th} voltage pulse burst. The jitter in the signals, recorded from the oscilloscope, is 2 ns. The voltage and current profiles are recorded with a Caltest CT4028 39 kV, 220 MHz high voltage probe and Pearson 2877 current monitor.

Fig. 1b shows a more detailed image of the powered electrode. It consists of a powered copper cylinder housed concentrically in a Delrin cylindrical block. A tapered mica cylinder is drilled into the copper to provide structural rigidity and to prevent discharge from leaking from the sides of the copper. A concentric channel is drilled into the mica to flow the He-H_2O mixture. Finally, a quartz dielectric with a center hole is fused to the copper and Delrin using an adhesive having high dielectric strength.

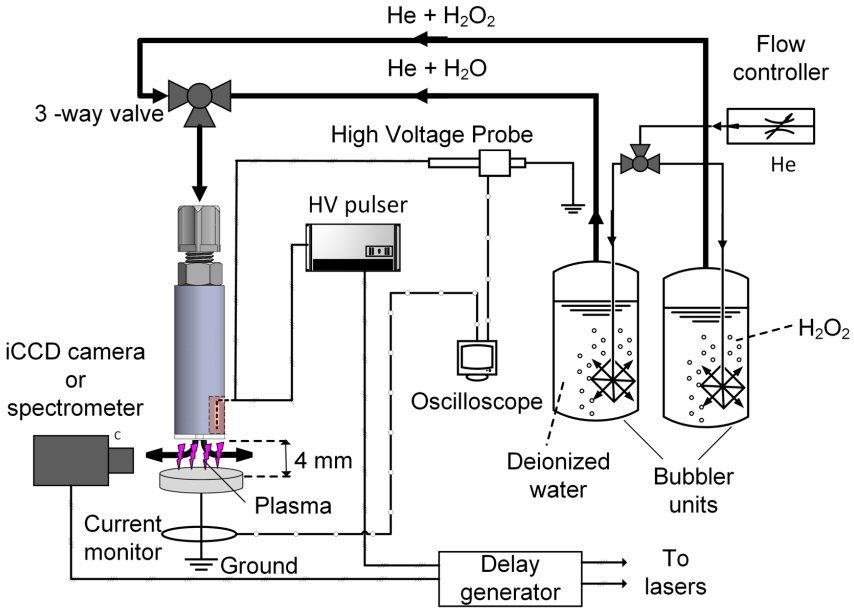

Figure 1a. Schematic of the plasma discharge setup

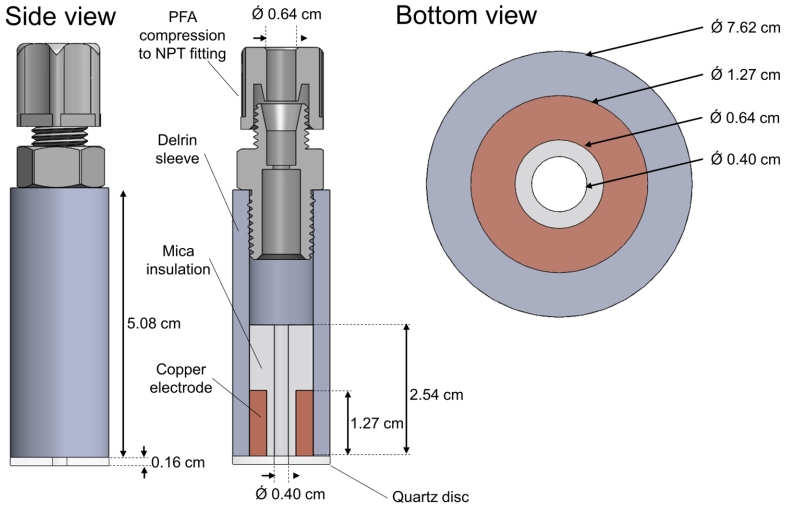

Figure 1b: Detailed configuration of the electrode

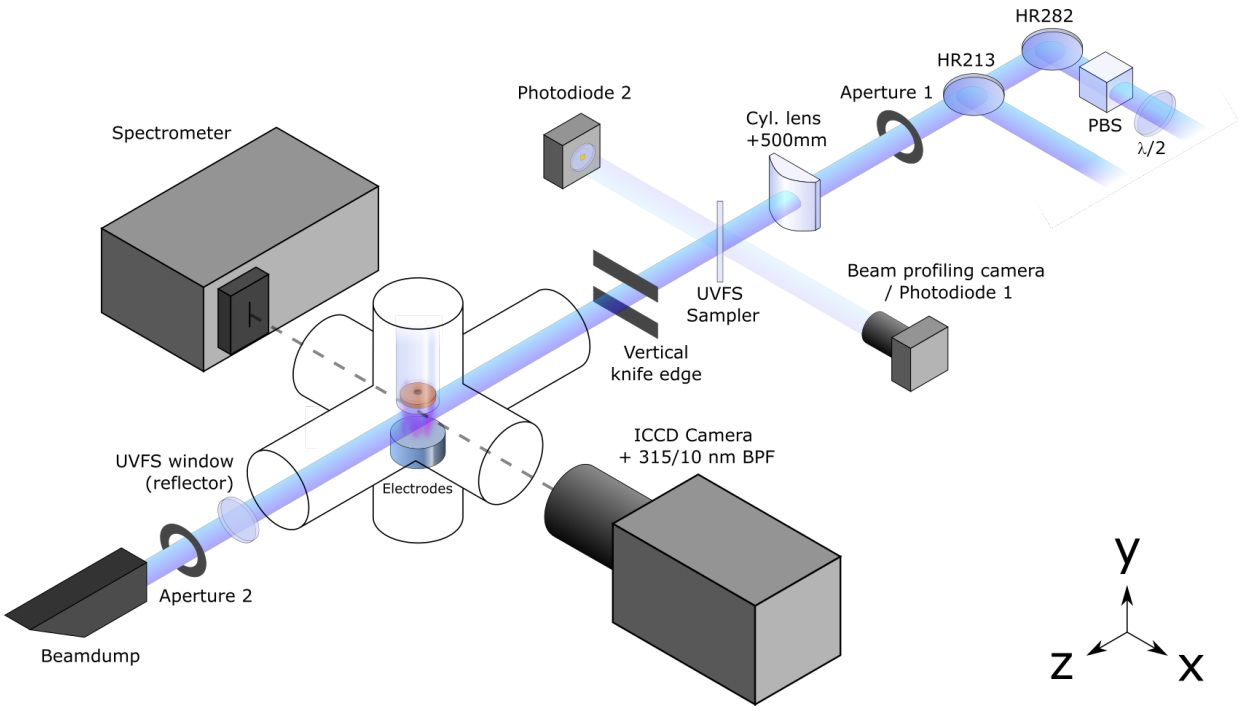

Figure 2: Experimental setup for PF-LIF detection

2.1 Optical setup

The optical layout for the detection of H_2O_2 and OH is shown in **Fig. 2**. H_2O_2 detection relies on a pump-probe scheme with the pump-laser photo-dissociating the H_2O_2 and the probe laser exciting laser-induced fluorescence of the resulting OH photo-fragments. For the pump laser, we employed the 5th harmonic of a Nd:YAG (Continuum Surelite) laser at 212.8 nm. Compared to previous H_2O_2 PF-LIF studies that used 248 nm and 266 nm for photo-dissociation, the increased absorption cross-section at 212.8 nm significantly outweighed the lower available beam energy, with $\sigma = 3.1 \cdot 10^{-19}$ cm^2 at 212.8 nm, versus $8.4 \cdot 10^{-20}$ cm^2 and $3.7 \cdot 10^{-20}$ cm^2 at 248 nm and 266 nm, respectively (*41*). At 212.8 nm, the major photo-fragments are ground-state OH radicals (*39*), and interference from water vapor is negligible because the H_2O absorption cross-section is at least five orders of magnitude lower than that of H_2O_2. The probe laser is a frequency-doubled dye laser (Lambda-Physik) with Rhodamine 6G dye pumped by the second harmonic Nd:YAG laser (Spectra Physics) to generate 281.996 nm (referred to as 282 nm in the rest of the paper). This beam excites the $Q_1(1)$ rotational level in the A-X(1,0) band, and fluorescence is detected from the A-X(1,1) and A-X(0,0) bands around 310 nm as in (*18*). The laser pulses are produced at a frequency of 10 Hz, with the probe laser delayed by 50 ns with respect to the pump laser. This delay prevents scattering and broadband fluorescence induced by the pump laser from interfering with the OH-LIF measurements

and is sufficiently short that the laser-produced OH does not significantly decay due to reactions within this delay time. This 50 ns delay is used throughout this work. The laser energy per pulse is 3.5 mJ for 212.8 nm beam, and 100 μJ – 400 μJ for 282 nm. This considerable spread is almost entirely due to long term drift between datasets that were acquired over a couple of days; the shot-to-shot variation of the LIF laser was ± 4%.

The laser beams are formed into vertical sheets focused at the center of the discharge using a cylindrical lens with a focal length of 500 mm. A knife-edge is used to crop the laser sheet to a height of 4 mm to reduce scattering from the electrode surfaces. A fused silica beam sampler reflects a small fraction of the incident laser beams to a beam profiling camera to record the beam profiles. The six-way quartz cross, which houses the electrode, has a flat entrance window and a Brewster angle exit window to prevent interference from a back-reflected beam. The OH-LIF signal from the DBD discharge is collected through one of the quartz windows and imaged onto an ICCD camera (Andor iStar) with a 45 mm focal length, f/1.8 UV camera lens. A bandpass filter with a central wavelength of 310 nm and an FWHM of 10 nm is placed in front of the camera to block laser scattering and reduce interference from plasma emission. Overlap between the two beams is optimized by aligning the beams to apertures and optimizing the PF-LIF signal in an H_2O_2 seeded flow.

The hydrogen peroxide mole fraction in the reference mixture is quantified by performing in-situ UV-absorption measurements directly in the 6-arm experimental cell (see section 3.1). Before the pump beam enters the experimental cell, the beam is sampled by a fused silica wedged plate. The beam profiler is replaced by a photodiode ("Photodiode 1" in **Fig. 2**) to record the reference beam intensity. After passing the cell once, part of the 212.8 nm beam is reflected by a fused silica window placed after the exit window. This reflector is removed from the beam path under normal operation. The reflected beam then passes through the cell a second time and is reflected by the fused silica wedged plate onto a second photodiode, "Photodiode 2". Both photodiodes are equipped with a diffuser to minimize the effect of small spatial fluctuations in the beam. The ratio of the signals of "Photodiode 2" over "Photodiode 1" is recorded for both an empty cell and a cell with the He-H_2O-H_2O_2 reference mixture.

2.2 Gas temperature measurement

The rotational temperature of OH (A, v'=1) is measured by spectrally resolving the fluorescence signal of the OH (A, v'=1) state after excitation of the $Q_1(1)$ transition in the electronic and vibrational ground state. Although a fit of the LIF excitation spectrum is usually a more reliable measure of the temperature, Verreycken et al [17] showed that the A-X(1,1) fluorescence spectrum yields similar values for the temperature in atmospheric pressure nanosecond pulsed discharges. The spectrally resolved fluorescence

signal is fitted by a synthetic spectrum generated from LIFBASE (*42*), with the rotational temperature obtained as one of the fitting parameters.

3. Absolute Calibration

3.1 Absolute calibration for H_2O_2

Absolute calibration of H_2O_2 PF-LIF signals is performed using He-H_2O-H_2O_2 reference mixtures with and without oxygen. The He-H_2O-H_2O_2 mixture is produced by flowing 2 slm of He through a (50 wt.%) hydrogen peroxide solution in a bubbler maintained at 283 K by the temperature-controlled water bath. The PF-LIF signals in the reference mixtures can be directly used for absolute calibration of the measurements in the plasma discharge provided that the collisional quenching rates are the same in the calibrations and experiments. Due to its low vapor pressure, the mole fraction of hydrogen peroxide vapor in the reference mixture is much smaller than that of water, so it may be assumed that quenching is dominated by water vapor in both the calibration and experiment. The water mole fraction is nominally the same in both cases, so collisional quenching rates of OH(A) in the reference mixture are the same as in the experiment and a separate fluorescence yield correction is not required.

Calibration of the absolute hydrogen peroxide mole fraction profile $\boldsymbol{x}_{HP}$ proceeds by calculating the ratio of PF-LIF signals in the experiment and reference mixture:

$$\boldsymbol{x}_{HP} = \frac{\boldsymbol{I}_{PFLIF} - \boldsymbol{I}_{LIF}}{\boldsymbol{I}^{ref}_{PFLIF} - \boldsymbol{I}^{ref}_{LIF}} x^{ref}_{HP}, \qquad \text{(Eq 1)}$$

where $\boldsymbol{I}_{PF-LIF}$ and $\boldsymbol{I}^{ref}_{PF-LIF}$ are the PF-LIF images in the experiment and reference mixture, respectively, $\boldsymbol{I}_{LIF}$ and $\boldsymbol{I}^{ref}_{LIF}$ are the background LIF images acquired using only the probe laser in the experiment and reference mixture, respectively, x^{ref}_{HP} is the H_2O_2 mole fraction in the reference mixture, and boldface symbols signify 2D images. The H_2O_2 mole fraction in the reference mixture was x^{ref}_{HP} = 560 ppm, which was determined from in-situ absorption measurements of the 212.8 nm laser beam using the double-pass setup described in section 2.1. The H_2O mole fraction from the bubbler was $x_{H_2O} = 1.5\%$, based on saturation of the bath gas at 600 Torr and 283 K. The submerged gas line in the bubbler is capped with a sintered thimble to reduce the bubble size and improve the contact surface area, which in addition to the lowered temperature guarantees that the gas flow is saturated with water.

3.2 Absolute calibration for OH

Absolute calibration of the OH-LIF images is accomplished in two steps; first, the LIF-signal $\boldsymbol{I}_{LIF}$ is normalized by the laser beam profile to correct for spatial variations in the laser intensity. The 282 nm laser

intensity profile is measured by seeding the flow with acetone and recording LIF signals of acetone excited by the 282 nm laser, $\boldsymbol{I}_{LIF}^{ace}$. In the second step, the normalized LIF-signal is multiplied by a scalar calibration constant C_{cal} to reflect absolute OH mole fractions. Combining the two steps yields an expression for the calibrated mole fraction profile $\boldsymbol{x}_{OH}$:

$$\boldsymbol{x}_{OH} = \frac{\boldsymbol{I}_{LIF}}{\boldsymbol{I}_{LIF}^{ace}} C_{cal}, \qquad \text{(Eq 2)}$$

The value of C_{cal} is determined by measuring the decay rate of OH that results from chemical reactions in a bath gas of known composition and temperature and matching it to the decay rate that is calculated with a chemical kinetic model, similar to the approach in (*13*). We measured the temporal decay of the LIF signals from OH produced by photo-fragmentation of H_2O_2 in the He-H_2O-H_2O_2 reference mixture at 293K, which provided a relatively clean system in which removal of OH is dominated by two reactions:

$$OH + OH \rightarrow H_2O + O \qquad \text{R1}$$

$$H_2O_2 + OH \rightarrow H_2O + HO_2 \qquad \text{R2}$$

The OH-decay trace is measured by recording LIF-images while stepwise increasing the delay time between the pump and probe laser pulses, starting at a delay of 50 ns and increasing in steps of 10 μs. Each of the LIF-images is first normalized by the laser profile, and then the LIF signal is averaged over a uniform region of the normalized image. The resulting LIF signal is plotted as a function of delay time with a logarithmic vertical scale in **Fig. 3**. The data in the plot is an average of measurements in the reference mixtures with and without oxygen. The addition of oxygen only made a 4% difference in the decay rate, although the magnitude of the LIF signals decreased with the addition of oxygen due to larger collisional quenching rates. The fluorescence yield ratio between the pure He and He + 5% O_2 admixture was measured to be Y_{O_2}/Y_{He} = 58%, which was used to correct the LIF intensity in the He-H_2O-O_2 mixture. The observed decay is nearly linear on the semi-log plot indicating that it is approximately a single exponential decay. This differs from the observed quadratic dependence of OH decay observed by Dilecce et al. (*13*) because the H_2O_2 concentration in our reference mixture is significantly higher than that of Dilecce, which results in the decay rate being dominated by the first-order (with respect to OH) reaction R2 instead of the second-order reaction R1.

Measurements of the reactive decay of OH are compared with simulations performed using the CHEMKIN code (*43*) to model the temporal decay of OH in a homogeneous mixture of the reference gas with the H_2/O_2 chemical kinetic mechanism of Li et al. (*44*). The initial conditions of the simulations are those of the reference experiment with a pressure of 600 Torr, a temperature of 293 K, and a mixture composition of $x_{He} = 0.985$, $x_{H2O} = 0.015$, $x_{H2O2} = 560$ ppm. The simulated OH decay is quite insensitive to the H_2O concentration, as expected from the dominant reactions (R1 and R2). The simulated OH decay curves were calculated using different initial OH mole fractions and compared to the measured OH decay.

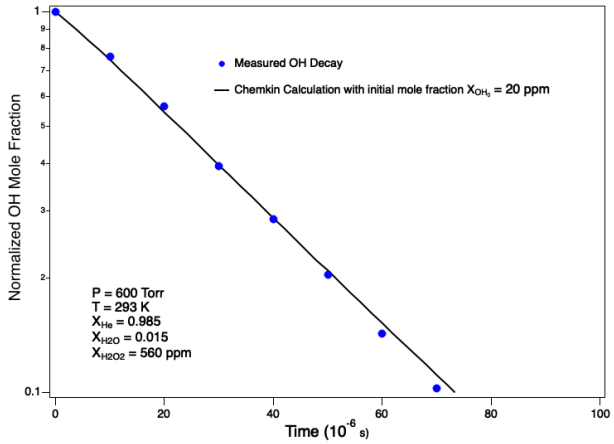

Figure 3: Comparison of measured and simulated OH(X) decay in a reference bath gas containing helium, water vapor, and hydrogen peroxide. A good match is obtained for an initial OH mole fraction of x_{OH}^{cal} = 20 ppm.

An initial OH mole fraction of 20 ppm provided the best match between the simulated and experimentally observed decays, as shown in **Fig. 3**.

The calibration constant in Eq. 2 is calculated as follows:

$$C_{cal} = x_{OH}^{cal}/y_0,$$

where, x_{OH}^{cal} is the 20 ppm OH mole fraction obtained by fitting the experiments with the CHEMKIN simulations, and y_0 is the OH-LIF signal in the reference gas mixture at a 50 ns time delay.

3.3 Saturation correction

At sufficiently high excitation laser energy, partial or even complete saturation of the LIF transition can occur, resulting in a sub-linear dependence of LIF signal intensity on the laser energy. The calibration procedure of the H_2O_2 profile is rather insensitive to partial saturation because the PF-LIF signals from the experiment $\boldsymbol{I}_{PFLIF}$ and reference $\boldsymbol{I}_{PFLIF}^{ref}$ have the same degree of saturation at a given position. As a result, spatial variations in the fluorescence yield are corrected for by the ratio $(\boldsymbol{I}_{PFLIF} - \boldsymbol{I}_{LIF})/(\boldsymbol{I}_{PFLIF}^{ref} - \boldsymbol{I}_{LIF}^{ref})$ in Eq 1. In contrast, the calibration procedure for OH-LIF measurements

in Eq. 2 does not account for saturation effects because the OH-LIF signal $\boldsymbol{I}_{LIF}$ is divided by the acetone LIF signal $\boldsymbol{I}_{LIF}^{ace}$ to correct for beam profile variations, and the acetone LIF signal is a linear function of laser fluence and does not capture the spatial variations in OH fluorescence yield.

To avoid artifacts in the OH measurements from spatial variations in the extent of saturation across the laser beam, we apply a non-linear mapping that accounts for the sub-linear dependence of the OH-LIF signal on the laser energy. The OH-LIF saturation curve shown in **Fig. 4** was measured by recording the LIF signal as a function of excitation laser energy. The energy was scanned using a variable attenuator, which was comprised of a rotating a half-wave waveplate in conjunction with a polarizing beam splitter cube. The laser energy was measured by a photodiode that was calibrated by comparing the diode signal to a laser power meter. The saturation curve is fitted with a function $f(E)$, which is a parabola with zero offset at the intercept, indicated by the black dashed curve in **Fig. 4**.

The fitted saturation function $f(E)$ is used to map the acetone-LIF image of the laser beam profile such that it contains the same non-linear energy dependence as the OH-LIF images and thus corrects for the spatial variations in signal due to OH-LIF saturation effects. To do so, we first convert the signal in the acetone-LIF image $\boldsymbol{I}_{LIF}^{ace}$ to a profile that can be used as input for the function $f(E)$. This beam energy profile image, $\boldsymbol{E}_{profile}$, is obtained by dividing $\boldsymbol{I}_{LIF}^{ace}$ by its spatial average and multiplying by the total measured beam energy of the excitation laser sheet E_0,

$$\boldsymbol{E}_{profile} = \frac{\boldsymbol{I}_{LIF}^{ace}}{\langle \boldsymbol{I}_{LIF}^{ace} \rangle} E_0, \tag{Eq 5}$$

such that the spatial average of $\langle \boldsymbol{E}_{profile} \rangle$ is equal to the beam energy E_0. We can now use $\boldsymbol{E}_{profile}$ as input to the saturation mapping function $f(E)$ and generate a mapped version of the acetone-LIF image $\tilde{\boldsymbol{I}}_{LIF}^{ace}$ that mimics the sub-linear energy dependence of the OH-LIF signal. The OH mole fractions are determined by substituting this mapped laser beam profile in Eq. 2 to normalize the OH-LIF images as follows:

$$\boldsymbol{x}_{OH} = \frac{\boldsymbol{I}_{LIF}}{\tilde{\boldsymbol{I}}_{LIF}^{ace}} C_{cal}, \tag{Eq 6}$$

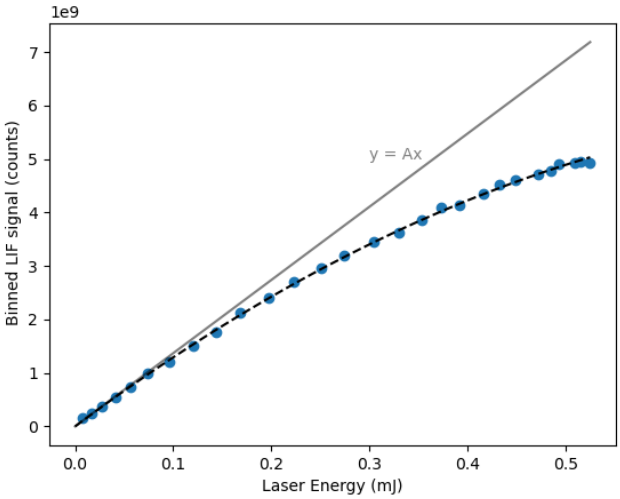

Figure 4: Dependence of OH-LIF signal on excitation laser energy. LIF measurements in the plasma used a laser excitation energy of up to 0.4 mJ, which requires corrections to account for partial saturation. The dashed line is a curve fit of the non-linear mapping function $f(E)$.

3.4 Considerations of laser-generated interference

In applications of photo-fragmentation LIF, consideration needs to be given to the species selectivity of the technique, which depends on the particular excitation-detection scheme as well as the composition and temperature of the gases within the probe volume. Direct interference could occur from a parent molecule other than H_2O_2 that photo-dissociates to produce additional ground state OH, which is then detected by LIF. In the plasmas considered here, the most likely direct interference would be photo-dissociaton of HO_2 by the 212.8 nm pump beam to form OH and atomic oxygen. The absorption cross-section of HO_2 at 212.8 nm for a temperature of 298 K is an order of magnitude higher than that of H_2O_2 (*45*). However, this larger cross-section is partially offset by the lower quantum yield of OH from HO_2 than from H_2O_2 (ϕ_{HO2}=1, ϕ_{H2O2}=1.5-2) (*39, 46, 47*). Another key consideration is the relative number densities of H_2O_2 and HO_2 in the plasma: the largest ratio of HO_2 to H_2O_2 is expected in the He-H_2O-O_2 plasma because the addition of O_2 to the He-H_2O mixture promotes formation of HO_2. A calculation of the species ratios that are expected in this plasma is beyond the scope of the present work, but previous kinetics modeling of nanosecond pulsed filament plasmas in an atmospheric pressure He-H_2O mixture with and without O_2 addition by Verreycken and Bruggeman provide some insights (*48*). They found that in a plasma with He+0.1% H_2O, the number density of H_2O_2 was at least two orders of magnitude larger than that of HO_2. In contrast, the addition of 0.1% O_2 produced a ratio of H_2O_2 to HO_2 closer to one order of magnitude. These results imply that HO_2 contributions to the PF-LIF signal could become significant in O_2-containing

mixtures. However, transient CHEMKIN calculations of the reactive decay of HO_2 in the mixtures used in the present studies indicate that HO_2 in the plasma afterglow decays much more rapidly than H_2O_2. As a result, any contribution from HO_2 to the PF-LIF signal in the He-H_2O-O_2 plasma would become negligible at most of the time delays used in this study.

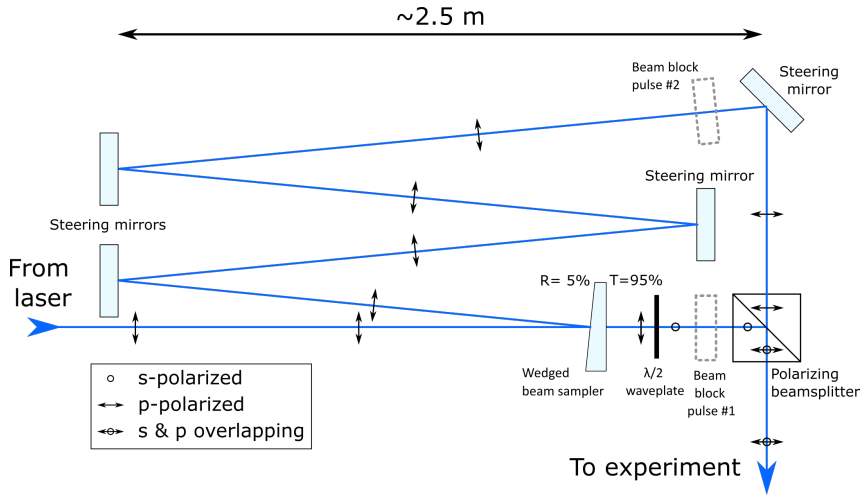

Figure 5: Delay stage used to test for photolytic interference by the 282 nm probe beam. We confirmed there was no significant interference (see text).

Another possible source of interference is photolytic production of OH by the LIF excitation laser, which could occur if plasma-generated species were photo-dissociated by the 282 nm beam. Early efforts to probe hydroxyl radicals in the atmosphere using 282 nm LIF excitation were plagued by such interferences that resulted from photo-dissociation of ozone to produce O(^{1}D), which reacts with water vapor to produce OH (*49, 50*). To test for photolytically produced OH in our plasma experiments, we performed a separate set of OH-LIF measurements using a different pump-probe configuration, as shown schematically in **Fig. 5**. A portion of the 282 nm beam was split off into a 30-ns delay line and then spatially overlapped with the undiverted portion of the beam using a waveplate and polarizing beam splitter. The undelayed portion of the beam contained 95% of the pulse energy and served as the pump pulse, while the delayed pulse contained 5% of the pulse energy and served as the probe. The image intensifier was gated during the delayed pulse and only detected OH-LIF signals from the probe pulse. The 30 ns pump-probe delay was sufficiently long to avoid detection of LIF signal from the pump pulse. If the pump pulse photolytically produced OH, then the OH-LIF signals from the probe beam would increase when the pump beam was present. However, the OH-LIF signals were nearly identical with and without blocking the pump beam, indicating that photolytic production of OH in the plasma in the He-H_2O mixture was negligible.

4. Results and discussions

4.1 Plasma emission

The optical emission for each pulse during the 5-pulse burst is shown sequentially in **Fig. 6** for the two mixtures studied. The emission images are recorded with the OH-LIF bandpass filter in place and an intensifier gate width of 50 ns, which captures the emission from a single pulse within the burst. For the

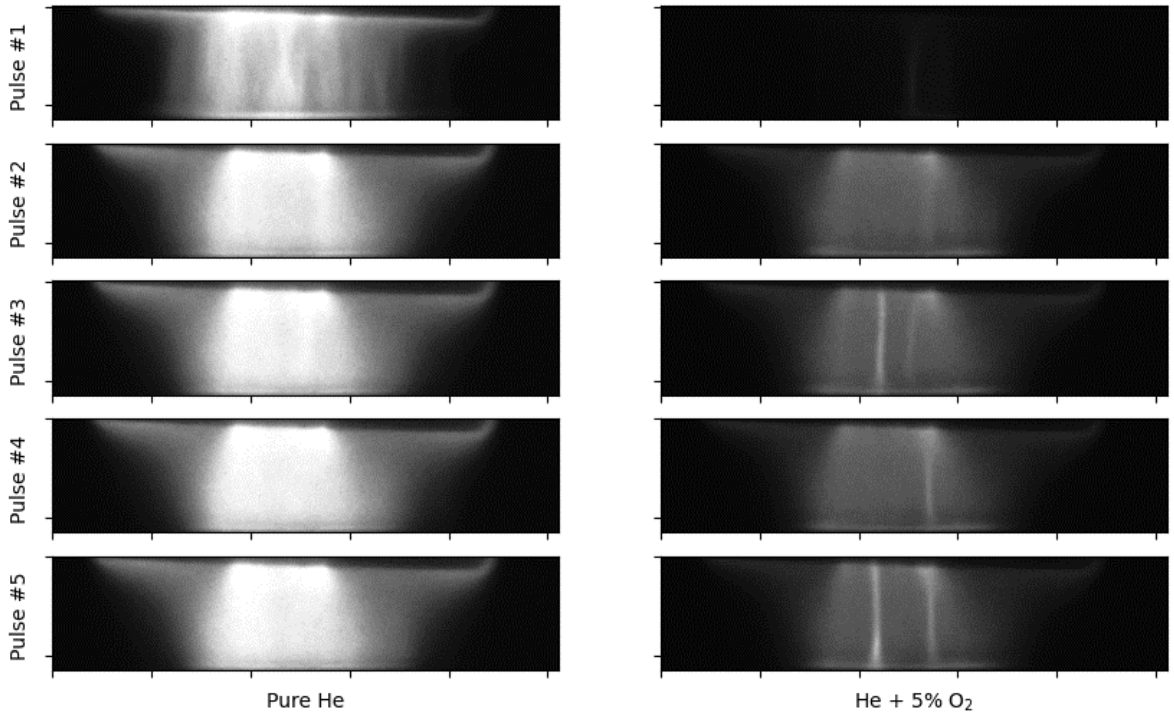

Figure 6: DBD emission in mixtures of pure He-H_2O (left) and (He + 5% O_2)-H_2O (right).

10-pulse burst, a pulse was generated every 10 μs instead of 20 μs. **Fig. 6** (left) shows the emission of a discharge in the H_2O-He mixture. The first pulse is filamentary, but successive pulses are more diffuse, and filaments are no longer observed. **Fig. 6** (right) shows the discharge emission for H_2O in He with a 5% admixture of O_2, using the same intensity scaling. For this mixture, almost no emission is visible during the first pulse, suggesting breakdown was hardly achieved. Pulses 2-5 show mostly diffuse emission with a few filaments superimposed. The diffuse part of the emission is approximately 30% as intense as the discharge in the He-H_2O-only mixture.

4.2 Measurement of gas temperature

The gas temperature was determined by recording OH-LIF fluorescence spectra in the 5-pulse plasma discharge at a series of time delays. The measured spectra were fitted by simulated LIF spectra from LIFBASE over a temperature range of 275K-300K. **Fig. 7** shows the measured fluorescence spectra as dots

in different colors for the different time delays. The black curve is a simulated spectrum at 300K, but the spectrum is not very sensitive to the temperature within the 275 K – 300 K temperature range. The fitting routine fits the A-X(1,1) and A-X(0,0) bands separately, although only the A-X(1,1) spectra are shown in the figure. The A-X(1,1) band contained the majority of the LIF signal intensity (95%), which is expected because the laser directly excites the A(v=1) state, whereas the A(v=0) state is populated by v=1→0 vibrational energy transfer.

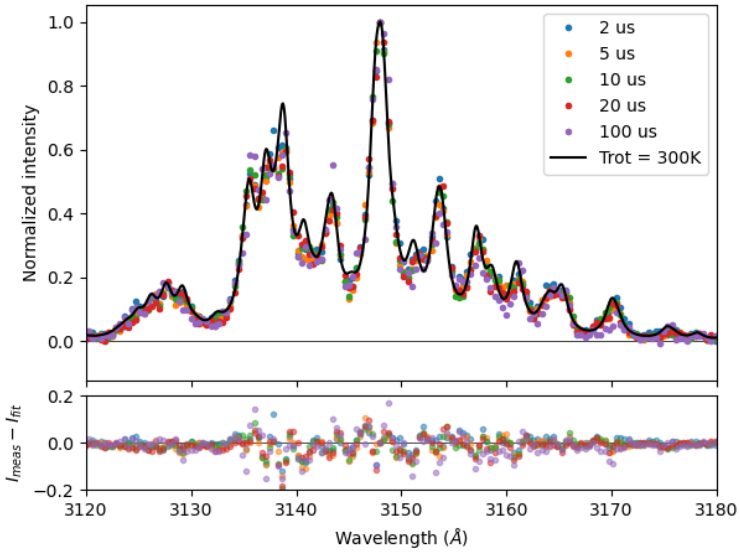

Figure 7: Measured fluorescence spectra (dots) in the plasma for a range of delay times. Obtained rotational temperatures are within 275-300K for all recorded time delays. The black curve displays the calculated spectrum at 300K; the spectrum at 275K does not differ appreciably from the 300K spectrum at this scale. The bottom part of the figure displays the residuals of the fit.

A comparison of the measured and simulated spectra shows that there is minimal heating of the gas by the plasma. This result is in line with expectations based on the coupled energy. Current, voltage, and coupled energy traces of the first pulse in a typical burst are displayed in the left plot of **Fig. 8**. The voltage

and current traces were used to determine the coupled energy, which is shown for each of the five pulses in the burst averaged over 100 bursts in the right plot. The average of the five pulses was 0.28 mJ per pulse or 1.4 mJ for the entire burst. To estimate gas heating by the plasma, we assume a cylindrical plasma volume 8 mm in diameter and 4 mm in height, based on the emission images. The 1.4 mJ of energy coupled into the plasma then translates to an enthalpy of 0.22 kJ/mol. If all this energy were put into gas heating, the temperature would only increase by 10 K.

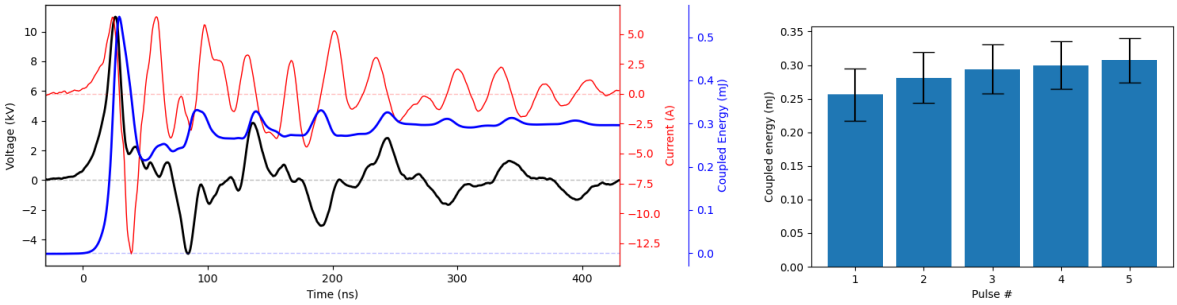

Figure 8: *Left:* Voltage, current, and coupled energy traces of the first pulse in a typical burst. *Right:* Mean coupled energy vs. pulse number in the burst averaged over 100 bursts. Error bars indicate standard deviation among the 100 bursts.

Fluorescence spectra from the PF-LIF measurements in the reference mixture of He-H_2O_2 without a plasma yielded very similar rotational temperatures and vibrational fractions, with no indication of higher vibrational levels being populated. This finding suggests that the OH produced by the photo-fragmentation process is fully equilibrated with the surrounding gas, which is consistent with previous observations by Johansson et al. (*33, 34*).

4.3 Temporally and spatially resolved measurements of OH and H_2O_2

The OH-LIF and H_2O_2 PF-LIF images were recorded at time delays ranging from 1 μs to 20 ms after the discharge burst. The (PF)-LIF signal was averaged over 100 laser shots for all images presented in this section. **Figs. 9a** and **9b** show the evolution of the OH and H_2O_2 profiles, respectively, for the He-H_2O mixture following the 5-pulse burst. At the shortest delay times, the OH distribution is concentrated in the mixing layer between the injected and surrounding gases with the peak values near the jet exit at the top of the imaged region. The OH slowly diffuses outward and onto the bottom surface, while, at the same time,

the mole fraction decays. Recording the H_2O_2 profile involves recording an image with both pump and probe lasers and subtracting the LIF from natively produced OH with only the probe laser. At delay times less than 500 μs, the H_2O_2 PF-LIF signal is significantly smaller than the LIF signal from native OH, and the H_2O_2 profiles cannot be resolved properly. At delay times of 500 μs and longer, the H_2O_2 profile clearly develops, and the same qualitative structure as in the OH profile can be observed. As expected, the decay time is much shorter for highly reactive OH radicals (~1 ms) than for the more chemically stable H_2O_2 (>10 ms). The H_2O_2 profile only becomes apparent when most of the OH has already decayed. A qualitative comparison between the profiles is facilitated by normalizing the OH profiles to their maximum value, shown in **Fig. 9c**. In these images, the similarities between the OH and H_2O_2 profiles are much more apparent: The H_2O_2 profile seems to mirror the OH profiles, although at longer time delays the central channel appears to be more clearly delineated in the H_2O_2 profiles. The normalized OH profiles clearly show that the central channel initially fills up with OH until 100 μs, and then the OH is displaced by freshly injected gas at 500 μs and 1 ms. The OH mole fractions ranging from 10 ppm at the edge to 60 ppm near the nozzle exit, measured 1 μs after the burst, are significantly higher than the ~1 ppm measured in (*21*) but are similar to the mole fractions measured in an RF glow discharge (*22*) and in a corona discharge (*25*), which both yielded around 15 ppm. Significantly higher mole fractions were obtained by (*51*) and (*27*), respectively 100 ppm and 1200 ppm, but both of these measurements were obtained in discharges without

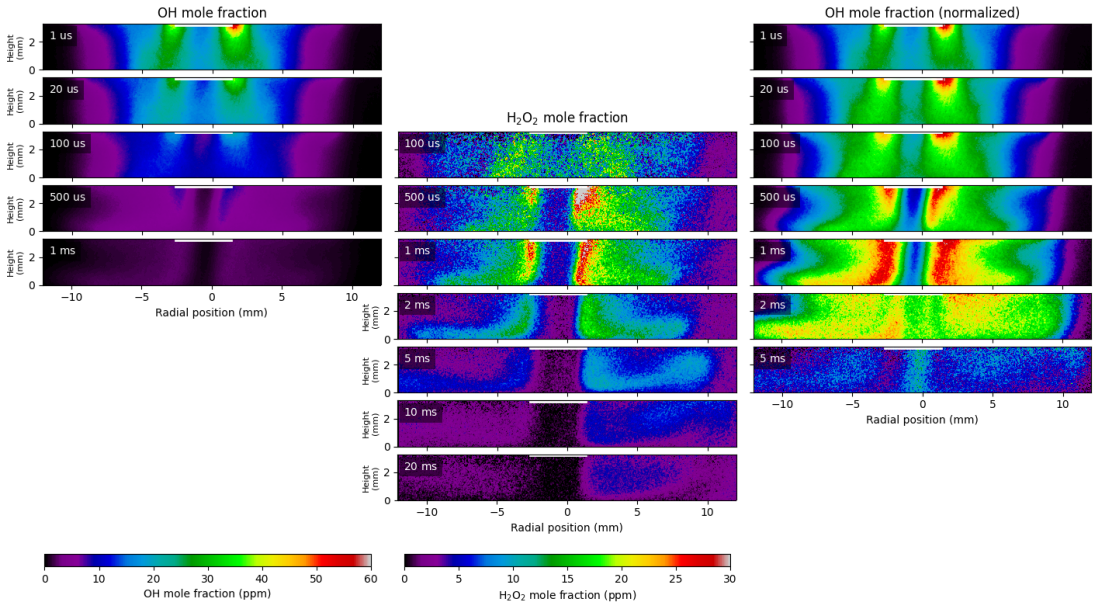

Figure 9: **(a)** OH and **(b)** H_2O_2 mole fraction profiles for 5-pulse burst in He-H_2O mixture. **(c)** Normalized OH-profiles showing the qualitative change in flow profile. The white bar at the top of each image indicates the nozzle exit.

any dielectric barrier, thus, plasma currents would have been significantly higher than in the present experiments.

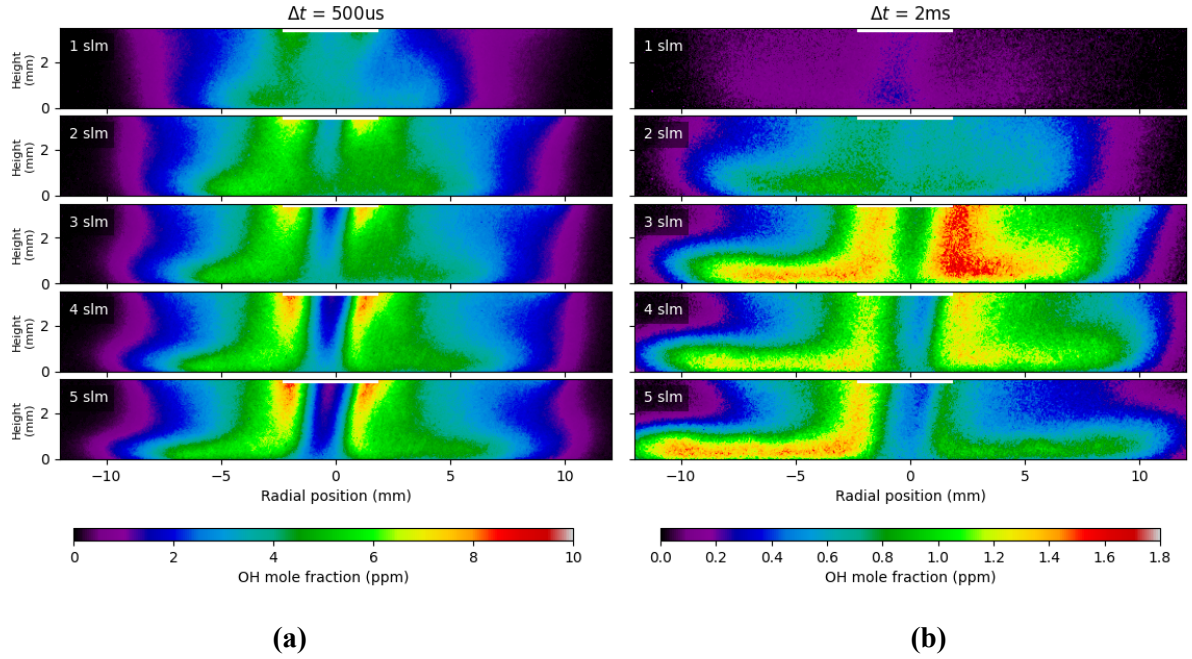

Figure 10: OH mole fraction profiles for a range of flow rates at **(a)** 500 μs and **(b)** 2 ms after the discharge burst.

The effect of the gas flow was further investigated by comparing profiles for different flow rates at fixed time delays. **Figs. 10a** and **10b** present the absolute OH-profiles in the 5-pulse, He-H_2O discharge, for delay times of 500 μs and 2 ms, respectively, at flow rates from 1 to 5 slm. At flow rates of 1 and 2 slm, the central jet is filled with OH radicals that have not been flushed out yet. At 3 slm, the OH is partially displaced by fresh gases, and at 4 and 5 slm, the center channel is mostly devoid of OH. This interpretation is consistent with estimates of the flow residence times, which are on the order of milliseconds. As the flow rates increase from 1 to 5 slm, the flow velocities increase proportionally thus decreasing the time required for fresh gases to displace plasma generated OH and H_2O_2. The higher flow rates also more effectively disperse the OH radicals along the surface, which is most evident at 2 ms. For larger flow rates, the stagnation flow is more clearly developed than for the lower flow rates.

Figs. 11a and **11b** show hydrogen peroxide profiles corresponding to the hydroxyl profiles in **Fig. 10**. For low flows, the profile appears to extend further horizontally than at higher flows, which could be the result of accumulated H_2O_2 from previous pulses. At larger flows, the H_2O_2 stays confined to the annulus around the jet exit and impinges on the surface, with a profile that is characteristic of a stagnation flow. At Δt = 2 ms, the progression of the H_2O_2 profile is qualitatively similar to the OH profiles (**Fig. 10b**), with

progressively more of the species flowing over the surface as the flow rate increases. Compared to OH, H_2O_2 is more concentrated around the center annulus. This could be explained by the fact that the H_2O_2 production rate is quadratic with respect to the OH concentration ($2OH \rightarrow H_2O_2$), and thus will show a sharper contrast than the OH-profile. The location of the peak OH concentration around the center annulus can be explained by the enhanced electric field near the central gas injection orifice due to sharp edges of the high voltage electrode. While the annular structure of the discharges is clearly revealed by the (PF-)LIF images, it is not as obvious from the emission images in **Fig. 6** because emission images are integrated over the line-of-sight.

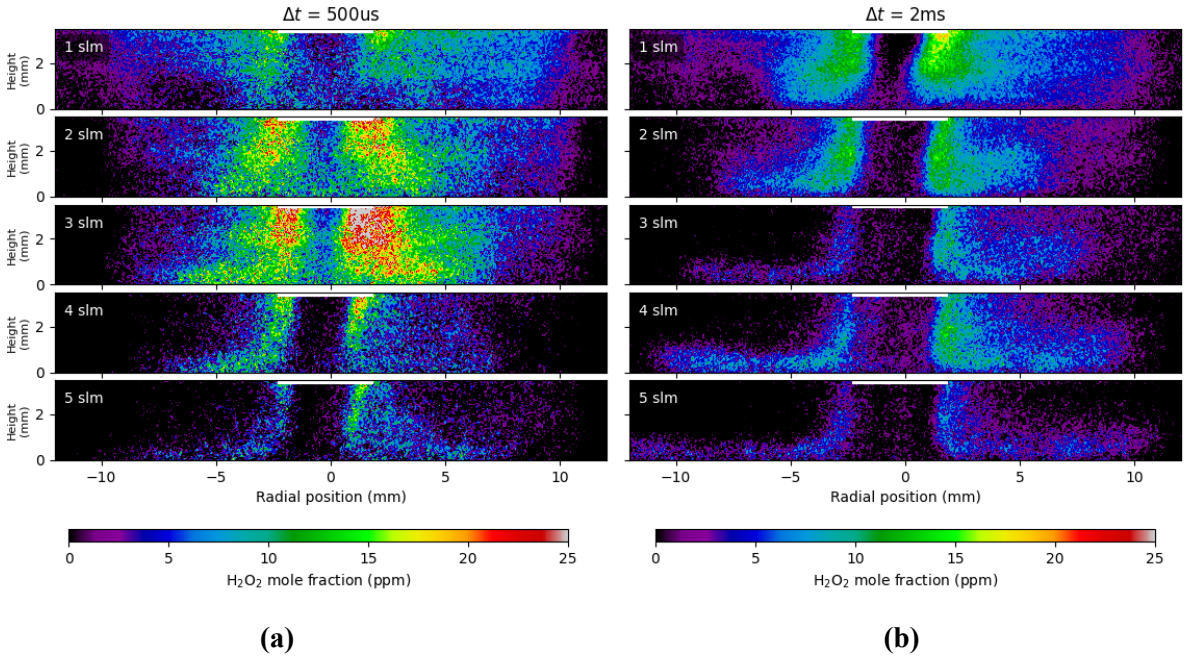

Figure 11: H_2O_2 mole fraction profiles for a range of flow rates at **(a)** 500 us and **(b)** 2 ms.

Images recorded as a function of delay time in the He-H_2O-O_2 mixture with an oxygen content of 5% at a flow rate of 4 slm are displayed in **Fig. 12a-c**. The OH mole fraction decays relatively quickly, but the peak OH mole fraction is approximately a factor of three lower than that in the He-H_2O mixture (20 ppm in **Fig. 12a** instead of 60 ppm in **Fig.9a**). At the earliest times, the hydrogen peroxide measurements in **Fig. 12b** are less stochastic and better resolved than those in **Fig. 9b**, probably because of the reduced interference from OH-LIF. At 100 μs, the profiles no longer show any stochastic behavior. Overall, the H_2O_2 production significantly increases with the addition of oxygen, resulting in a five times greater peak H_2O_2 mole fraction (150 ppm in **Fig. 12b** compared to 30 ppm in **Fig. 9b**). Furthermore, the peak H_2O_2 mole fraction occurs at an earlier time in the sequence with oxygen addition (1 μs in **Fig. 12b** compared to 500 μs in **Fig. 9b**). The evolution of the OH profiles is more clearly seen in the peak-normalized images in

Fig. 12c. From these images, it is clear that the H_2O_2 profiles mirror the OH profiles reasonably well, at least qualitatively. As time progresses, the H_2O_2 profile appears more concentrated near the mixing layer at the boundary of the central helium jet, while the OH profile expands radially and spans a larger fraction of the imaged region.

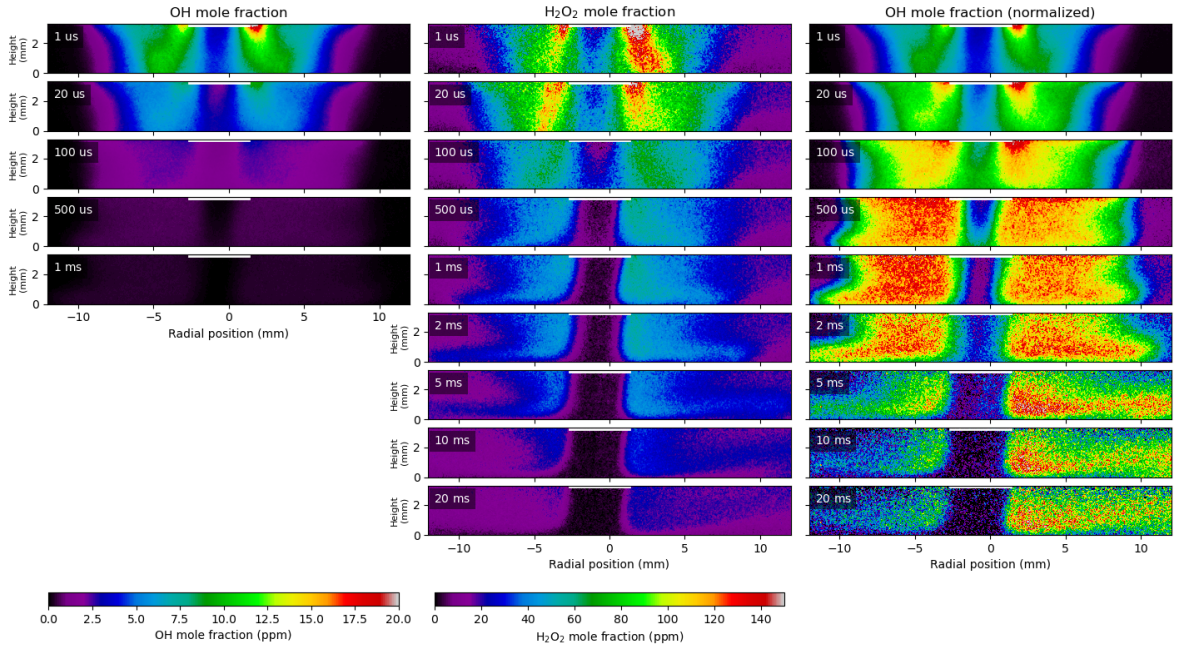

Figure 12: **(a)** OH and **(b)** H_2O_2 mole fraction profiles for 5-pulse burst in He-H_2O-O_2 mixture. **(c)** Normalized OH-profiles showing the qualitative change in flow profile. The white bar at the top indicates the nozzle exit.

We next considered the effect of increasing the number of pulses in the discharge from 5 to 10. The overall evolution of OH and H_2O_2 profiles for the 10-pulse discharge is qualitatively similar to that of the 5-pulse discharge. The comparison of the 5 and 10-pulse discharges focuses on the shorter time scales for OH and the longer time scales for H_2O_2. **Figure 13a-d** shows the OH and H_2O_2 profiles at 1 μs and 2 ms delays, respectively, for the gas mixtures both with and without oxygen. In the He-H_2O mixture, the additional pulses significantly increased the production of H_2O_2 but had less of an effect on the OH mole fraction. In contrast, for the He-H_2O-O_2 mixture, the 10-pulse discharge increased the OH mole fraction but somewhat decreased the H_2O_2 mole fraction.

The effects of increasing the number of pulses in the discharge and adding O_2 depend on a series of coupled reaction pathways. In a He-H_2O system without O_2, the typical reaction channels that produce OH have low energy requirements and include $e + H_2O \rightarrow e + OH + H$, $\Delta E_{Threshold} = 7.62$ eV; $e + H_2O \rightarrow OH +$

H^-, $\Delta E_{Threshold}$ = 5.30 eV; $e + H_2O \rightarrow OH^- + H$, $\Delta E_{Threshold}$ = 4.30 eV (*52*). The energy requirement to generate OH from negative hydroxyl ions OH^- is even lower $e + OH^- \rightarrow OH + 2e$, $\Delta E_{Threshold}$ = 3.37 eV. The presence of energetic electrons in the plasma therefore sustains the formation of OH in the system. The dominant consumption pathways for OH include the formation of H_2O_2 and recombination to water through $2OH + He \rightarrow H_2O_2 + He$, $2OH \rightarrow H_2O + O$ and $H + OH + He \rightarrow H_2O + He$ (*52*). These consumption reactions are driven by neutral species and are independent of the electrons. An increase in the number of discharge pulses is expected to increase the electron density, which would enhance OH production through the aforementioned pathways, leading to increased H_2O_2 production. This process is consistent with the observations in **Figs. 9** and **12**, but the increase in OH is not apparent in **Fig. 13**.

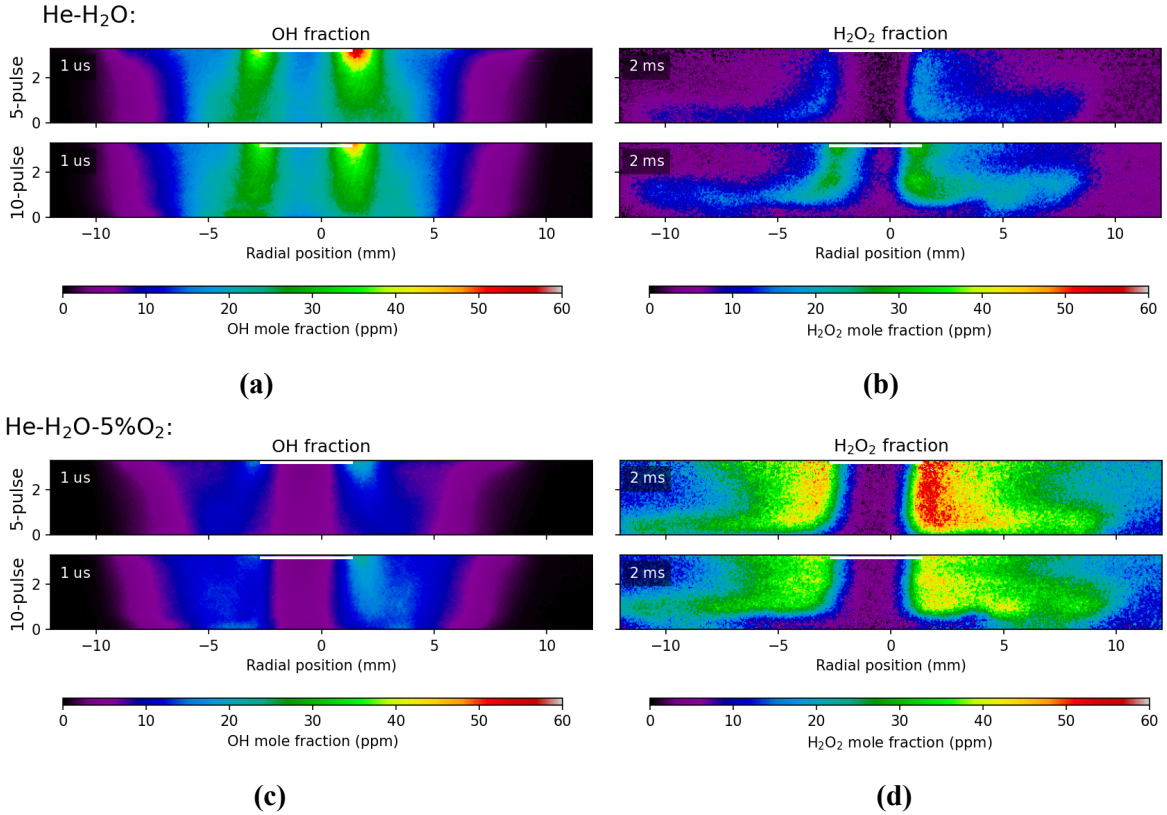

Figure 13: Comparison of OH and H_2O_2 mole fractions without oxygen addition (top two rows, **a** and **b**) and with oxygen (bottom two rows, **c** and **d**), for the 5-pulse (upper) and 10-pulse bursts (lower).

The effects of O_2 addition can vary depending on the plasma conditions (*48*). Molecular oxygen is dissociated in the plasma via reactions: $e + O_2 \rightarrow 2O + e$, $\Delta E_{Threshold}$ = 6.00 eV; $e + O_2 \rightarrow O(^1D) + O(^3P) + e$, $\Delta E_{Threshold}$ = 8.40 eV. The resulting generation of $O(^1D)$ and $O(^3P)$ affects the formation and consumption of OH and H_2O_2 through a series of reaction pathways, such as OH formation through reaction with water vapor $H_2O + O(^1D) \rightarrow 2OH$, consumption of OH by $OH + O(^1D) \rightarrow O_2 + H$ or $OH + O \rightarrow O_2 + H$, and

consumption of H_2O_2 through $H_2O_2 + O(^1D) \rightarrow H_2O + O_2$. Verreycken et al. (*48*) found that the addition of O_2 to an atmospheric pressure He-H_2O nanosecond pulsed filament plasma caused a temporary increase in the consumption of OH via the reaction $OH + O \rightarrow O_2 + H$ as well as increased production of H, HO_2, and H_2O_2. The additional HO_2 subsequently led to enhanced OH production in the late afterglow. Sankaranarayanan et al. found that addition of up to 3% O_2 in an argon DBD plasma increased OH production, but further addition of O_2 decreased OH production due to electron attachment to O_2 and reaction of OH with ozone via $OH + O_3 \rightarrow HO_2 + O_2$, (*53*). Both the work of Verreycken and Sankaranarayanan indicate that there exists an optimum concentration of O_2 that allows OH to reach a maximum value, and further increases in O_2 result in a decrease of OH as O_2 and its associated excited, dissociated, and recombination products compete for species that contribute to the production of OH and H_2O_2.

In the present experiments, the O_2 addition results in an overall decrease in OH mole fraction, but a subsequent increase farther downstream is not observed. The additional coupled energy provided by 10 pulses could introduce a combination of effects; OH production is enhanced by increased rates of dissociation and dissociative attachments to H_2O, while atomic oxygen production is also enhanced by dissociation of O_2. For the conditions studied here, the net result is an enhanced OH production.

In contrast, the overall H_2O_2 mole fractions in **Fig. 13** increase with O_2 addition but become relatively insensitive to additional discharge pulses. This result suggests that there may be compensating formation and consumption reactions that limit the effect of additional coupled energy on H_2O_2 in the presence of admixed O_2. For example, the net increase in OH could promote formation of H_2O_2, while the formation of additional excited-state atomic oxygen could increase consumption of H_2O_2 via $H_2O_2 + O(^1D) \rightarrow H_2O + O_2$. A more complete mechanistic understanding will require a detailed kinetics simulation.

5. Summary

Atmospheric pressure non-thermal plasma discharges produce reactive species that react with biological samples, making these discharges suitable for biomedical devices and plasma medicine. The presence of water vapor significantly impacts the formation of reactive species, and quantitative in-situ imaging measurements are needed to provide insights into the distributions of these species. In this work, the spatiotemporal evolution of two key reactive species, H_2O_2 and OH, was investigated in a canonical dielectric barrier plasma source that provides a well-defined flow-field in the form of a stagnation plane. The plasma source enables in-situ generation of OH and H_2O_2 by controlling the water vapor concentration in the system. The feasibility of spatially and temporally resolved quantitative detection of H_2O_2 was

demonstrated using photo-fragmentation laser-induced fluorescence (PF-LIF). The H_2O_2 PF-LIF measurements were calibrated using *in-situ* UV-absorption spectroscopy in a reference gas mixture containing H_2O_2. In addition, we calibrated absolute OH-LIF profiles by coupling kinetic modeling with measurements of the reactive decay of OH after photo-fragmentation of H_2O_2 in the reference mixture.

Hydrogen peroxide and hydroxyl profiles were recorded in a He-H_2O mixture by bubbling helium gas through a temperature-controlled water bubbler. Profiles obtained in the afterglow of a discharge in this mixture were compared to those in a He-H_2O-O_2 mixture which had 5% O_2 admixed. In the oxygen admixed mixture, peak OH mole fractions decreased by approximately a factor of 3, while H_2O_2 mole fractions increased by approximately a factor of 5 compared to the He-H_2O mixture. Increasing the number of pulses from 5 to 10 per burst increased both OH and H_2O_2 mole fractions in the He-H_2O mixture. In the He-H_2O-O_2 mixture, the additional pulses increased the OH mole fractions but did not significantly change the H_2O_2 mole fractions, suggesting that competing reactions moderate the H_2O_2 production when additional coupled energy is provided in the presence of oxygen.

Time-resolved images of the OH profiles revealed that OH radicals mostly decayed after 1 ms, while H_2O_2 was still present at significant mole fractions after 5 ms. The mole fraction profiles of OH and H_2O_2 tend to be concentrated in an annulus around the plasma discharge at short time scales and evolve into a typical stagnation flow profile as time progresses. The measurements show that the non-thermal plasma source is an effective tool to impinge a surface with hydrogen peroxide and hydroxyl radicals and by extension is expected to be suitable for surface treatments in decontamination and biomedical applications. These measurements provide an understanding of the spatiotemporal evolution of two key species in the active plasma. In many applications, reactive species will exit the plasma source and transit into an effluent region where they will mix with the ambient surrounding – and the kinetics will differ due to the involvement of different gases. While these processes are not considered in this work, the presented results provide a basis for further work on understanding reactive species kinetics. The measured species profiles also will serve as validation targets in a canonical plasma configuration.

Acknowledgements

MT and TF acknowledge the support from the Emerging Frontiers and Multidisciplinary Activities (EFMA) of US National Science Foundation under Grant No. 2029425. This material is based upon work supported by the U.S. Department of Energy, Office of Science, Office of Fusion Energy Sciences. This research used resources of the Low Temperature Plasma Research Facility at Sandia National Laboratories, which is a collaborative research facility supported by the U.S. Department of Energy,

Office of Science, Office of Fusion Energy Sciences. This article has been authored by an employee of National Technology & Engineering Solutions of Sandia, LLC under Contract No. DE-NA0003525 with the U.S. Department of Energy (DOE). The employee owns all right, title and interest in and to the article and is solely responsible for its contents. The United States Government retains and the publisher, by accepting the article for publication, acknowledges that the United States Government retains a non-exclusive, paid-up, irrevocable, world-wide license to publish or reproduce the published form of this article or allow others to do so, for United States Government purposes. The DOE will provide public access to these results of federally sponsored research in accordance with the DOE Public Access Plan *https://www.energy.gov/downloads/doe-public-access-plan*.

References

1. E. Ceriani, E. Marotta, V. Shapoval, G. Favaro, C. Paradisi, Complete mineralization of organic pollutants in water by treatment with air non-thermal plasma. *Chem. Eng. J.* **337**, 567-575 (2018).
2. R. Ma *et al.*, Non-thermal plasma-activated water inactivation of food-borne pathogen on fresh produce. *J. Hazards Mater.* **300**, 643-651 (2015).
3. B. Penetrante *et al.*, Identification of mechanisms for decomposition of air pollutants by non-thermal plasma processing. *Plasma Sources Sci. Technol.* **6**, 251 (1997).
4. K. Y. Baik *et al.*, Non-thermal plasma jet without electrical shock for biomedical applications. *Appl. Phys. Lett.* **103**, 164101 (2013).
5. S. Kalghatgi *et al.*, Effects of non-thermal plasma on mammalian cells. *PLoS One* **6**, e16270 (2011).
6. Y. H. Kim *et al.*, Measurement of reactive hydroxyl radical species inside the biosolutions during non-thermal atmospheric pressure plasma jet bombardment onto the solution. *Plasma Chem. Plasma Process.* **34**, 457-472 (2014).
7. B. Ghimire *et al.*, The influence of a second ground electrode on hydrogen peroxide production from an atmospheric pressure argon plasma jet and correlation to antibacterial efficacy and mammalian cell cytotoxicity. *J. Phys. D: Appl. Phys.* **55**, 125207 (2021).
8. J. Karuppiah *et al.*, Abatement of mixture of volatile organic compounds (VOCs) in a catalytic non-thermal plasma reactor. *J. Hazards Mater.* **237**, 283-289 (2012).
9. M. Magureanu, N. B. Mandache, V. I. Parvulescu, Degradation of pharmaceutical compounds in water by non-thermal plasma treatment. *Water Res.* **81**, 124-136 (2015).
10. A. M. Vandenbroucke, R. Morent, N. De Geyter, C. Leys, Non-thermal plasmas for non-catalytic and catalytic VOC abatement. *J. Hazards Mater.* **195**, 30-54 (2011).
11. D. Yan *et al.*, The Correlation Between the Cytotoxicity of Cold Atmospheric Plasma and the Extracellular H2O2-Scavenging Rate. *IEEE Trans. Radiat. Plasma Med. Sci.* **2**, 618-623 (2018).
12. J. H. Frank, Advances in imaging of chemically reacting flows. *J. Chem. Phys.* **154**, 040901 (2021).
13. G. Dilecce, P. Ambrico, M. Simek, S. De Benedictis, LIF diagnostics of hydroxyl radical in atmospheric pressure He-H2O dielectric barrier discharges. *Chem. Phys.* **398**, 142-147 (2012).
14. K. Tachibana, T. Nakamura, Characterization of dielectric barrier discharges with water in correlation to productions of OH and H2O2 in gas and liquid phases. *Jpn. J. Appl. Phys.* **58**, 046001 (2019).

15. R. Ono, X. Zhang, A. Komuro, Effect of oxygen concentration on the postdischarge decay of hydroxyl density in humid nitrogen-oxygen pulsed streamer discharge. *J. Phys. D: Appl. Phys.* **53**, 425201 (2020).
16. L. Feng, Y. Zhuang, C. Haijing, F. Zhi, W. Wenchun, The investigation of OH radicals produced in a DC glow discharge by laser-induced fluorescence spectrometry. *Plasma Sci. Technol.* **23**, 064002 (2021).
17. C. Winters *et al.*, OH radical kinetics in hydrogen-air mixtures at the conditions of strong vibrational nonequilibrium. *J. Phys. D: Appl. Phys.* **50**, 505203 (2017).
18. T. Verreycken, R. Van der Horst, A. Baede, E. Van Veldhuizen, P. Bruggeman, Time and spatially resolved LIF of OH in a plasma filament in atmospheric pressure He–H2O. *J. Phys. D: Appl. Phys.* **45**, 045205 (2012).
19. N. Shirai, H. Owada, K. Sasaki, Efficient production and transport of OH radicals in spatial afterglow of atmospheric-pressure DC glow discharge using intersecting helium flows. *Plasma Sources Sci. Technol.* **30**, 125012 (2021).
20. Y. Yang, Y. Zhang, Z. Liao, X. Pei, S. Wu, OH radicals distribution and discharge dynamics of an atmospheric pressure plasma jet above water surface. *IEEE Trans. Radiat. Plasma Med. Sci.* **2**, 223-228 (2017).
21. X. Pei, S. Wu, Y. Xian, X. Lu, Y. Pan, On OH density of an atmospheric pressure plasma jet by laser-induced fluorescence. *IEEE Trans. Plasma Sci.* **42**, 1206-1210 (2014).
22. P. Bruggeman, G. Cunge, N. Sadeghi, Absolute OH density measurements by broadband UV absorption in diffuse atmospheric-pressure He–H2O RF glow discharges. *Plasma Sources Sci. Technol.* **21**, 035019 (2012).
23. Y. Du, G. Nayak, G. Oinuma, Z. Peng, P. J. Bruggeman, Effect of water vapor on plasma morphology, OH and H2O2 production in He and Ar atmospheric pressure dielectric barrier discharges. *J. Phys. D: Appl. Phys.* **50**, 145201 (2017).
24. R. Ono, T. Oda, OH radical measurement in a pulsed arc discharge plasma observed by a LIF method. *IEEE Trans. Ind. Appl.* **37**, 709-714 (2001).
25. R. Ono, T. Oda, Measurement of gas temperature and OH density in the afterglow of pulsed positive corona discharge. *J. Phys. D: Appl. Phys.* **41**, 035204 (2008).
26. S. Kanazawa *et al.*, LIF imaging of OH radicals in DC positive streamer coronas. *Thin Solid Films* **515**, 4266-4271 (2007).
27. T. Verreycken, R. Van Der Horst, N. Sadeghi, P. Bruggeman, Absolute calibration of OH density in a nanosecond pulsed plasma filament in atmospheric pressure He–H2O: comparison of independent calibration methods. *J. Phys. D: Appl. Phys.* **46**, 464004 (2013).
28. T. Verreycken, P. J. Bruggeman, OH density measurements in nanosecond pulsed discharges in atmospheric pressure N2–H2O mixtures. *Plasma Sources Sci. Technol.* **23**, 015009 (2014).
29. T. Verreycken, N. Sadeghi, P. J. Bruggeman, Time-resolved absolute OH density of a nanosecond pulsed discharge in atmospheric pressure He–H2O: absolute calibration, collisional quenching and the importance of charged species in OH production. *Plasma Sources Sci. Technol.* **23**, 045005 (2014).
30. H. L. Wapshott-Stehli, B. G. Myers, M. J. Herrera Quesada, A. Grunden, K. Stapelmann, Plasma-driven biocatalysis: In situ hydrogen peroxide production with an atmospheric pressure plasma jet increases the performance of OleTJE when compared to adding the same molar amount of hydrogen peroxide in bolus. *Plasma Process. Polym.*, e2100160 (2022).
31. C. J. Aul, M. W. Crofton, J. D. Mertens, E. L. Petersen, A diagnostic for measuring H2O2 concentration in a shock tube using tunable laser absorption near 7.8 μm. *Proc. Combust. Inst.* **33**, 709-716 (2011).

32. D. Z. Pai, Plasma-liquid interfacial layer detected by in situ Raman light sheet microspectroscopy. *J. Phys. D: Appl. Phys.* **54**, 355201 (2021).
33. O. Johansson, J. Bood, M. Aldén, U. Lindblad, Detection of hydrogen peroxide using photofragmentation laser-induced fluorescence. *Appl. Spectrosc.* **62**, 66-72 (2008).
34. B. Li *et al.*, Quantitative detection of hydrogen peroxide in an HCCI engine using photofragmentation laser-induced fluorescence. *Proc. Combust. Inst.* **34**, 3573-3581 (2013).
35. B. Li, D. Zhang, M. Yao, Z. Li, Strategy for single-shot CH3 imaging in premixed methane/air flames using photofragmentation laser-induced fluorescence. *Proc. Combust. Inst.* **36**, 4487-4495 (2017).
36. K. Larsson *et al.*, Instantaneous imaging of ozone in a gliding arc discharge using photofragmentation laser-induced fluorescence. *J. Phys. D: Appl. Phys.* **51**, 135203 (2018).
37. J. Bradshaw *et al.*, Photofragmentation two-photon laser-induced fluorescence detection of NO2 and NO: Comparison of measurements with model results based on airborne observations during PEM-Tropics A. *Geophys. Res. Lett.* **26**, 471-474 (1999).
38. D. van den Bekerom, C. Richards, E. Huang, I. Adamovich, J. H. Frank, 2D imaging of absolute methyl concentrations in nanosecond pulsed plasma by photo-fragmentation laser-induced fluorescence. *Plasma Sources Sci. Technol.* **31**, 095018 (2022).
39. G. L. Vaghjiani, A. A. Turnipseed, R. F. Warren, A. Ravishankara, Photodissociation of H2O2 at 193 and 222 nm: Products and quantum yields. *J. Chem. Phys.* **96**, 5878-5886 (1992).
40. K. Larsson, O. Johansson, M. Aldén, J. Bood, Simultaneous visualization of water and hydrogen peroxide vapor using two-photon laser-induced fluorescence and photofragmentation laser-induced fluorescence. *Appl. Spectrosc.* **68**, 1333-1341 (2014).
41. L. T. Molina, M. J. Molina, UV absorption cross sections of HO2NO2 vapor. *J. Photochem.* **15**, 97-108 (1981).
42. J. Luque, D. R. Crosley, LIFBASE: Database and spectral simulation program (version 1.5). *SRI international report MP* **99**, (1999).
43. R. Kee *et al.*, CHEMKIN collection, release 3.6, reaction design. *Inc., San Diego, CA* **20**, 0 (2000).
44. J. Li, Z. Zhao, A. Kazakov, F. L. Dryer, An updated comprehensive kinetic model of hydrogen combustion. *Int. J. Chem. Kinet.* **36**, 566-575 (2004).
45. S. Sander *et al.*, *Chemical kinetics and photochemical data for use in atmospheric studies: evaluation number 15*. (Pasadena, CA: Jet Propulsion Laboratory, California Institute of Technology, 2010).
46. A. Sinha, J. Coleman, R. Barnes, Photodissociation Dynamics of HO2 at 220 nm: Determination of the O (1D): O (3P) Branching Ratio. *J. Phys. Chem.* **98**, 12462-12465 (1994).
47. L. Lee, Observation of O (1 D) produced from photodissociation of HO2 at 193 and 248 nm. *J. Chem. Phys.* **76**, 4909-4915 (1982).
48. T. Verreycken, P. Bruggeman, OH dynamics in a nanosecond pulsed plasma filament in atmospheric pressure He–H2O upon the addition of O2. *Plasma Chem. Plasma Process.* **34**, 605-619 (2014).
49. D. E. Heard, M. J. Pilling, Measurement of OH and HO2 in the troposphere. *Chem. Rev.* **103**, 5163-5198 (2003).
50. C. C. Wang, L. Davis Jr, C. Wu, S. Japar, Laser-induced dissociation of ozone and resonance fluorescence of OH in ambient air. *Appl. Phys. Lett.* **28**, 14-16 (1976).
51. O. Li *et al.*, Active species generated by a pulsed arc electrohydraulic discharge plasma channel in contaminated water treatments. *Plasma Chem. Plasma Process.* **32**, 343-358 (2012).
52. S. Schröter *et al.*, Chemical kinetics in an atmospheric pressure helium plasma containing humidity. *Phys. Chem. Chem. Phys.* **20**, 24263-24286 (2018).
53. R. Sankaranarayanan, B. Pashaie, S. Dhali, Laser-induced fluorescence of OH radicals in a dielectric barrier discharge. *Appl. Phys. Lett.* **77**, 2970-2972 (2000).